

Article

Predicting Melt Pond Fraction on Landfast Snow Covered First Year Sea Ice from Winter C-Band SAR Backscatter Utilizing Linear, Polarimetric and Texture Parameters

Saroat Ramjan ¹, Torsten Geldsetzer ¹ , Randall Scharien ²  and John Yackel ^{1,*}

¹ Cryosphere Climate Research Group, Department of Geography, University of Calgary, Calgary, AB T2N 1N4, Canada; saroot.ramjan@ucalgary.ca (S.R.); geldsetz@ucalgary.ca (T.G.)

² Department of Geography, University of Victoria, Victoria, BC V8W 2Y2, Canada; randy@uvic.ca

* Correspondence: yackel@ucalgary.ca

Received: 28 June 2018; Accepted: 2 October 2018; Published: 9 October 2018



Abstract: Early-summer melt pond fraction is predicted using late-winter C-band backscatter of snow-covered first-year sea ice. Aerial photographs were acquired during an early-summer 2012 field campaign in Resolute Passage, Nunavut, Canada, on smooth first-year sea ice to estimate the melt pond fraction. RADARSAT-2 Synthetic Aperture Radar (SAR) data were acquired over the study area in late winter prior to melt onset. Correlations between the melt pond fractions and late-winter linear and polarimetric SAR parameters and texture measures derived from the SAR parameters are utilized to develop multivariate regression models that predict melt pond fractions. The results demonstrate substantial capability of the regression models to predict melt pond fractions for all SAR incidence angle ranges. The combination of the most significant linear, polarimetric and texture parameters provide the best model at far-range incidence angles, with an R^2 of 0.62 and a pond fraction $RMSE$ of 0.09. Near- and mid- range incidence angle models provide R^2 values of 0.57 and 0.61, respectively, with an $RMSE$ of 0.11. The strength of the regression models improves when SAR parameters are combined with texture parameters. These predictions also serve as a proxy to estimate snow thickness distributions during late winter as higher pond fractions evolve from thinner snow cover.

Keywords: melt pond fraction; snow; SAR; polarimetric parameters; GLCM texture

1. Introduction

The spatial distribution, evolution, and extent of melt ponds on sea ice are functions of snow thickness and snow redistribution processes through the preceding winter and spring, ice surface roughness, and ice type [1–4]. For spatially varying snow covers on sea ice, thicker snow takes longer to melt than thinner snow under consistent atmospheric forcing [1,5,6]. Prior studies advocate that a thinner snow cover leads to dominant surface flooding (i.e., larger areal melt pond fraction, f_p), whereas a thick winter snow cover leads to a greater fraction of snow patches and thus less surface flooding (i.e., smaller f_p) [7,8]. Thicker snow covers generally accumulate on comparatively rough first-year sea ice (FYI), as the uneven surface topography effectively captures wind-blown snow [9]. The relatively smooth topography of FYI causes thinner snow covers, with consistent drifting of snow following the wind direction during depositional storm events [10]. Therefore, smooth FYI, with an associated thin snow cover, leads to the horizontal spreading of ponds over a larger area, with f_p as high as 80% [3,4,11]. Since the formation of FYI melt ponds is influenced by winter snow thickness, f_p could provide a proxy for winter ice surface roughness and snow thickness.

After melt onset, melt ponds gradually develop over four successive stages. These stages have been previously identified as: (1) topographic control, (2) hydrostatic balance, (3) ice freeboard control and (4) fall freeze up or ice break up [6,8,12]. During stage 1, melt ponds start to form and eventually fill topographic depressions with minimal drainage through the ice. At this stage, the structure of the melt ponds is very unstable and is actually controlled by the pre-melt ice topography [1]. Stage 2 begins when melt ponds have the same production and drainage rates, and lateral melt water flows towards macroscopic fractures and seal holes promote the formation of melt pond networks by interconnecting melt ponds. Consequently, the geometric structure of melt pond covers becomes prominent during this stage [1,12]. Stage 3 is characterized by increased vertical drainage and decreased horizontal discharge to macroscopic fractures. Surface topography of melting and decaying ice cover controls the melt pond coverage in this stage [6]. Finally, during stage 4, complete decay or disintegration of FYI, or fall freeze up of multiyear sea ice begins.

Estimating melt pond fraction over large areas requires satellite-based methods. Optical approaches [13–18] are hampered by cloud cover and are thus limited by the accuracy of cloud identification and screening techniques. They must also contend with regional differences in spectral properties [18], and issues related to sub-pixel variation. The root-mean-squared error (RMSE) for optical approaches is 0.08 to 0.16. Approaches using passive microwave data [19] are limited by the sensor resolution, especially in narrow channels where land contamination is likely. They are also only applicable to very high sea ice concentrations; even small areas of open water would dominate the signal.

Approaches using active microwave data have provided varying results. Barber and Yackel [20] report a relationship between ERS-1 backscatter and f_p , but note a limitation related to wind roughening of melt ponds. Mäkynen et al. [21] report poor skill in connecting changes in f_p with backscatter magnitude and texture using ENVISAT WSM images of sea ice during the ponding stages. Scharien et al. [22] report on the usefulness of co-polarization and cross-polarization ratios in estimating f_p during ponding using RADARSAT-2 quad-pol data; their RMSE values range from 0.05 to 0.43. Using TerraSAR-X, Fors et al. [23] also find the co-polarization ratio useful during the ponding stage, at intermediate wind speeds, with an RMSE is 0.4; they also evaluate four polarimetric parameters and find reasonable correlations. To evaluate prediction of f_p from winter images, Scharien et al. [24,25] use ENVISAT-ASAR and Sentinel-1 co- and cross-polarized backscatter and texture measures thereof. They report overall RMSE values of 0.08 and 0.09, but acknowledge model underestimation of f_p for smooth FYI related to sensor noise floors.

Estimating melt pond fraction over smaller areas and for validation of the techniques above rely on in-situ observations [11,22], or low-level aerial photographs [26,27]. A recent study using low-level aerial photographs showed that, due to their fine spatial and temporal resolutions, they are an ideal data source for estimating f_p since image classification accuracies are as high as 97% [22].

Using winter imagery to predict f_p implies an association of sea ice roughness and/or its snow cover variability with subsequent f_p . Comprehensive studies on the degree of winter snow thickness spatial variability, as well as relationships with f_p , are essential to better understand radiative transfer processes leading to snow and sea ice ablation rates during the spring melt transition. However, studying snow thickness variability on sea ice is complicated. The accumulation and redistribution of snow on FYI exhibits high spatio-temporal variability [9], and logistical challenges, resulting in a shortage of in-situ data [10]. Snow thickness distributions have been obtained in-situ [9,28–30], using laboratory-based procedures [31,32], and using remote sensing methods based on passive microwave data [33–35], frequency-modulated continuous-wave airborne radar returns [36,37] and Synthetic Aperture Radar (SAR) data [7,38,39], and using a combination of active microwave scatterometer and optical data [40].

The use of SAR backscatter must also contend with variability in backscatter with incidence angle (θ). Kim et al. [41] identified the θ effect on backscatter intensity, as it strongly influences surface

and volume scattering processes. Microwaves are dominated by surface scattering at lower θ ($<30^\circ$); whereas at higher θ ($>30^\circ$), volume scattering dominates over surface scattering [42,43].

The advent of polarimetric SAR data provide additional parameters for characterizing sea ice surfaces. Polarimetric parameters such as the Co-polarized phase difference, Co-polarized correlation coefficient, Entropy, Anisotropy, and Alpha angle can be calculated from second-order derivatives of the scattering matrix (i.e., covariance and coherency) to obtain enhanced information about both surface and volume scattering mechanisms of snow and sea ice [39,44–47].

In addition to linear and polarimetric parameters, SAR image texture also provides valuable structural information, leading to higher winter sea ice classification accuracy when compared to backscatter intensity alone [48–51]. Second-order texture measures, derived from the gray-level co-occurrence matrix (GLCM) introduced by Haralick et al. [52], were evaluated for sea ice classification [49], showing that the combination of σ^0 (tone/grey-level) and texture measures (spatial dependence in tone) gives better results than using texture measures alone. GLCM texture is the most commonly used texture analysis technique; as it takes into account the spatial organization of grey tones within a moving window and offers a second-order statistical technique for extracting texture features [49,52]. Image texture of snow covered sea ice is a function of its near surface characteristics e.g., snow properties, snow thickness variability, and ice roughness [53]. Several studies successfully demonstrated the potential of GLCM texture measures, calculated from SAR images, to improve classification/segmentation of snow covered sea ice [49,51,53,54].

Given that the most consistent skill in estimating f_p is reported by winter prediction of f_p [24], we build on the winter prediction technique in this paper. We maintain the use of texture parameters as in Mäkynen et al. [21] and Scharien et al. [24] and expand on the analysis by evaluating the contributions of polarimetric parameters as per Fors et al. [23], and we assess texture measures of the polarimetric parameters. Furthermore, given the relationship of winter snow thickness and subsequent f_p , we attempt an initial inversion of f_p to estimate snow thickness.

Objectives

The primary objective of this study is to predict early summer f_p from winter C-band SAR polarimetric backscatter. A secondary objective is to relate the predicted f_p to the spatial distribution of snow thickness. Meeting these objectives will aid in understanding the relationship between snow thickness variability on FYI during winter and its evolution into a melt pond icescape in early summer. Since the SAR backscatter coefficient σ^0 is largely a function of θ , this study will also examine the θ dependency on backscatter and its relationship with f_p . The following research questions towards these objectives are stated:

1. What are the relationships between winter C-band RADARSAT-2 (RS-2) SAR backscatter (linear and polarimetric parameters and texture parameters) and f_p ?
2. How does the relationship between RS-2 SAR backscatter and f_p change with θ ?
3. Can we predict f_p based on linear, polarimetric and texture parameters, and can predicted f_p be used to infer the late winter snow thickness variability?

2. Methodology

2.1. Study Area

The study area is located in Resolute Passage, Nunavut, Canada and comprises of a large area of landfast FYI. The study area was imaged by the RADARSAT-2 SAR satellite during late-winter and by aerial photography during the melt pond season (Figure 1). Analyzing the melt pond evolution stages, we consider that stage 2 is a suitable time to examine aerial images of f_p and its relationship with late winter snow thickness. In-situ observations were carried out from late-winter through the melt pond season at a field site ~4 km southwest of Sheringham Point, Cornwallis Island. Fieldwork was conducted in two coordinated sampling periods (Legs). Leg 1 field work was conducted during

the late-winter/early-spring period (8 to 29 May 2012), while Leg 2 was during late-spring/summer (4 June to 2 July 2012). Melt-onset was observed on 1 June 2012. Throughout Leg 1, the snow thickness range in the study region was 1.5 cm to 40 cm. Snow depths from snow pits and 5 transect lines 100 to 150 m long were collected. One snow depth measurement was acquired from each pit (a total of 102), and 565 snow depth measurements were sampled from all transects at 1 m spatial intervals. For this study, we used 202 samples of snow depth, including 102 measurements from the snow pits, and 100 measurements randomly selected from the snow transects to minimize spatial autocorrelation (Figure 2a) [9]. SAR acquisitions and snow samples were obtained at air temperatures between $-20\text{ }^{\circ}\text{C}$ and $-3\text{ }^{\circ}\text{C}$ (Figure 2b). An autonomous 2.75 m tall micro-meteorological station was installed on the sea ice from 18 May to 25 June 2012 to monitor air temperature, wind speed, and direction at 1-min intervals.

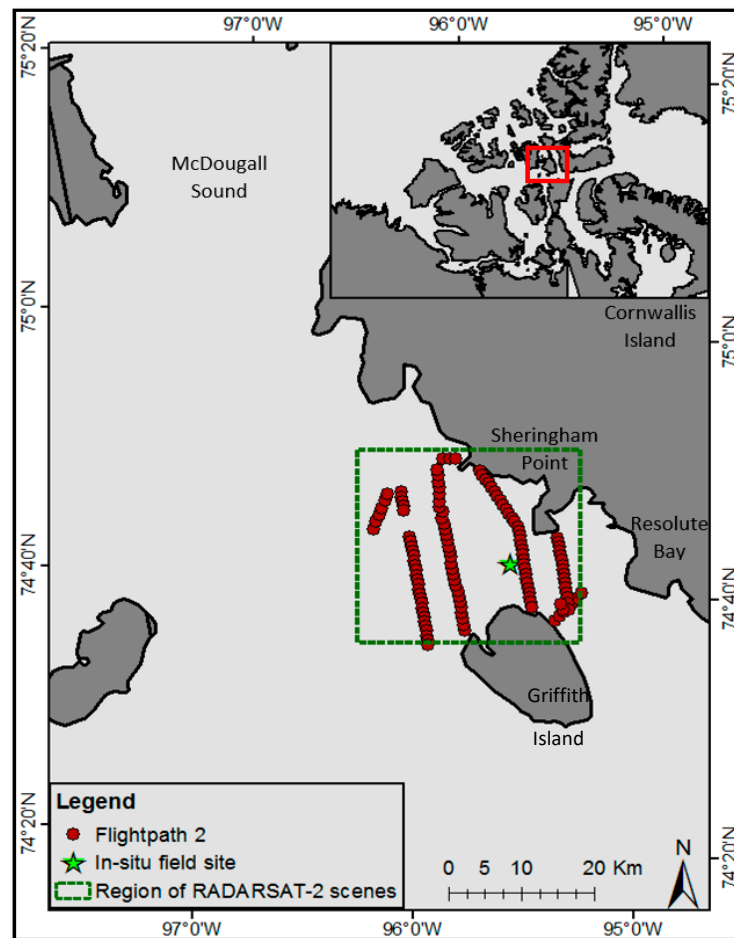


Figure 1. Study area in Resolute Passage, Nunavut, illustrating the in-situ field site, the flightpath of the aerial survey, and the region covered by RADARSAT-2 scenes. The red box in the inset map of the Canadian Arctic Archipelago delineates the location of the study area.

2.2. Data

2.2.1. Aerial Surveys

In early summer, the field site was initially characterized by a very shallow and wet snow cover overlying a rough superimposed ice layer. Melt ponds started to form on 10 June 2012, were fully formed on 15 June reaching at a maximum pond fraction of 78%, and remained above 50% until 25 June [12]. To quantify the evolution of melt ponds, their morphology, and f_p at a regional scale, four aerial photography surveys were flown between 13 and 29 June 2012 via fixed-wing *Twin Otter*

aircraft. A Canon G10 camera attached to an opening in the hindmost of the plane acquired digital optical images at nadir viewing angle, with a sampling rate resulting in 0% to ~10% image overlap. Data from the second survey flight on 22 June 2012, 01:43 UTC (Figure 1) are used in this study, while the melt ponds were fully formed and the geometric structures of the melt ponds were established. The survey was flown at an altitude of 610 m in a grid pattern that also coincided with the field study site. The image data has a swath width of 750 m and pixel size of 0.22 m [22]. At the time of acquisition, the surface air temperature was approximately 2.6 °C, and the melt ponds were liquid and moderately wind roughened over the entire region; the wind speed was 3.2 m/s at the on-ice meteorological station and 5.3 m/s at the Resolute weather station.

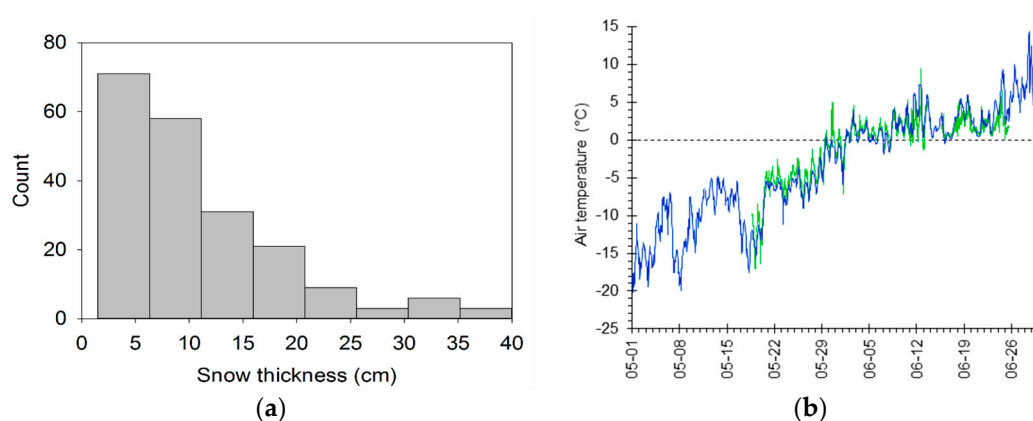


Figure 2. (a) Distribution of 202 in-situ snow thickness measurements collected on FYI acquired from the field site during Leg 1. (b) Hourly air temperature at the Resolute CARS weather station, Nunavut (blue), and once a minute on-ice air temperature (green).

2.2.2. RADARSAT-2 Data

RS-2 SAR scenes were acquired in fine quad-pol mode over the aerial flightpath at near-range (18° – 29°) (NR), mid-range (30° – 39°) (MR) and far-range (40° – 49°) (FR) θ . Each scene consists of a polarimetric (HH + VV + HV + VH and inter-channel phase information) data set, with a nominal $5.2\text{ m} \times 7.7\text{ m}$ resolution in range and azimuth, respectively, and covers a $25\text{ km} \times 25\text{ km}$ area (MDA, 2014). This study uses seven RS-2 scenes acquired during Leg 1, that encompass the majority of aerial photographs of melt ponded sea ice acquired during Leg 2 (Table 1).

Table 1. 25 km by 25 km RS-2 scenes used in this study and the number of 750 m by 750 m aerial photographs that fall within each SAR scene.

SAR Scene	Acquisition Date (yyyy-mm-dd)	Incidence Angle (Range)	Number of Aerial Photographs
FQ4	2012-05-10	23.1° (NR)	78
FQ8	2012-05-24	27.8° (NR)	97
FQ13	2012-05-21	33.2° (MR)	97
FQ15	2012-05-21	35.2° (MR)	87
FQ18	2012-05-18	38.1° (MR)	102
FQ22	2012-05-17	41.7° (FR)	87
FQ23	2012-05-15	42.6° (FR)	102

2.3. Methods

2.3.1. Estimation of Melt Pond Fraction from Aerial Photographs

f_p was calculated from aerial photographs using a decision-tree classification approach [22]. Melt ponds are distinguished from adjacent ice/snow patches because the albedo of ponds is

significantly lower than the snow and/or ice. The resulting classification (e.g., Figure 3a) has an error of 0.03 [22]. The distribution of f_p for the 22 June 2012 flightpath is presented in Figure 3b.

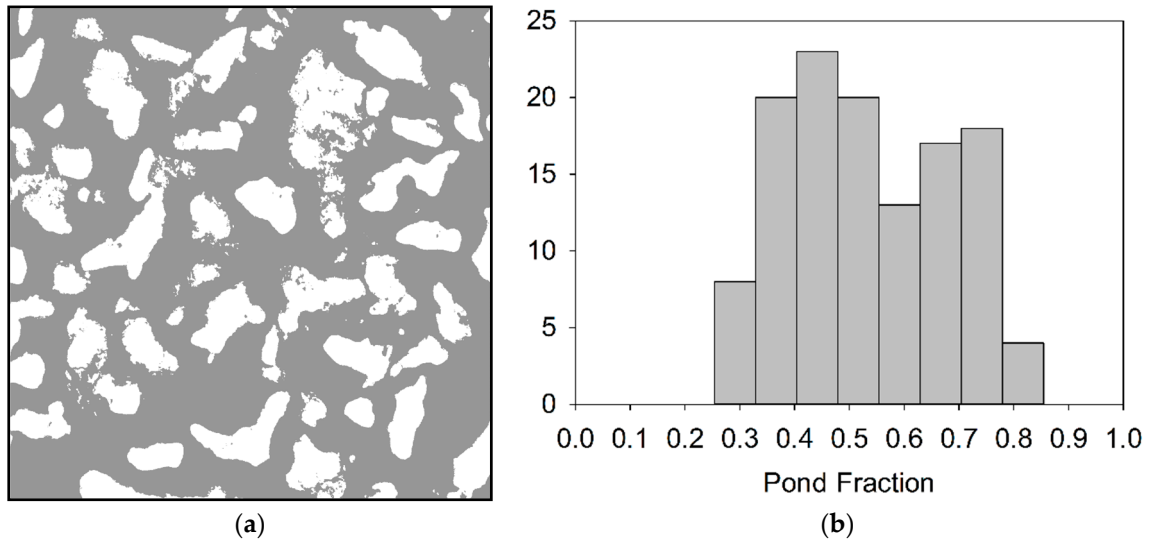


Figure 3. (a) Sample of a classified aerial photograph with melt ponds (grey areas) and snow patches (white areas); (b) histogram of pond fraction distribution for the flightpath on 22 June 2012.

2.3.2. RADARSAT-2 Data Processing

RS-2 data were calibrated, and speckle filtered using a 5×5 boxcar filter to reduce the speckle effect while preserving image information [55,56]. Four linear and five polarimetric parameters were derived (Table 2). Polarimetric parameters were derived from covariance (1) and coherency matrices (2), as applicable [57,58]. Eight GLCM texture parameters (Table 3) were calculated for each linear and polarimetric parameter (Table 2) using a 5×5 moving window. Therefore, a total of 81 parameters (image bands) were generated. All parameter images were projected to a common geographic coordinate system using nearest neighbor intensity interpolation, at 5 m pixel spacing.

$$[C] = \begin{bmatrix} \langle |S_{HH}|^2 \rangle & \sqrt{2} \langle S_{HH} S_{HV}^* \rangle & \langle S_{HH} S_{VV}^* \rangle \\ \sqrt{2} \langle S_{HV} S_{HH}^* \rangle & 2 \langle |S_{HV}|^2 \rangle & \sqrt{2} \langle S_{HV} S_{VV}^* \rangle \\ \langle S_{VV} S_{HH}^* \rangle & \sqrt{2} \langle S_{VV} S_{HV}^* \rangle & \langle |S_{VV}|^2 \rangle \end{bmatrix} \quad (1)$$

$$[T] = \begin{bmatrix} \langle |(S_{HH} + S_{VV})|^2 \rangle & \langle (S_{HH} + S_{VV})(S_{HH} - S_{VV})^* \rangle & 2 \langle (S_{HH} + S_{VV}) S_{HV}^* \rangle \\ \langle (S_{HH} - S_{VV})(S_{HH} + S_{VV})^* \rangle & 2 \langle |(S_{HH} - S_{VV})|^2 \rangle & 2 \langle (S_{HH} - S_{VV}) S_{HV}^* \rangle \\ 2 \langle S_{HV} (S_{HH} + S_{VV})^* \rangle & 2 \langle S_{HV} (S_{HH} - S_{VV})^* \rangle & 4 \langle |S_{HV}|^2 \rangle \end{bmatrix} \quad (2)$$

2.3.3. Image Sampling

Polygons corresponding to each 750 m by 750 m aerial photograph were used to extract spatially coincident SAR backscatter statistics from the seven RS-2 SAR scenes. The number of samples varied according to the portions of the RS-2 scenes that overlapped aerial photographs (Table 1). The total number of samples is 650, distributed across three different θ ranges.

Sample means of the nine linear and polarimetric parameters and eight GLCM parameters were calculated. Therefore, each of the 650 samples contains 81 associated mean values, corresponding to the nine linear and polarimetric parameters and their 72 derived texture parameters. Given that many adjacent aerial photographs overlap each other by up to approximately 10%, not all samples are entirely independent. However, the sample means and texture parameters represent the polygons as a whole, with no single-sample redundancy. Samples were divided into two equally sized training

and test sets using a random sampling approach. A set of 325 training samples were used for model development, and 325 test samples were used to validate the derived models.

Table 2. Parameters employed in this study. Matrix elements are obtained from a standard covariance matrix (1) and coherency matrix (2) (Adapted from Gill et al., 2015).

Nomenclature	Notation	Reference
Co-polarized power (horizontal) (in dB)	σ_{HH}^0 (linear)	[57]
Co-polarized power (vertical) (in dB)	σ_{VV}^0 (linear)	
Cross-polarized power (in dB)	σ_{HV}^0 (linear)	
Co-polarized ratio (in dB)	$R_{VVHH} = \frac{\langle S_{VV}S_{VV}^* \rangle}{\langle S_{HH}S_{HH}^* \rangle}$ (linear)	
Co-polarized phase difference	$\phi = \tan^{-1} \left[\frac{\text{Im}\langle S_{HH}S_{VV}^* \rangle}{\text{Re}\langle S_{HH}S_{VV}^* \rangle} \right]$ (polarimetric)	
Co-polarized correlation co-efficient	$\rho = \left \frac{\langle S_{HH}S_{VV}^* \rangle}{\sqrt{\langle S_{HH}S_{HH}^* \rangle \langle S_{VV}S_{VV}^* \rangle}} \right $ (polarimetric)	
Entropy	H (polarimetric)	[58]
Anisotropy	A (polarimetric)	
Alpha angle	α (polarimetric)	

Table 3. GLCM texture parameters used in the study.

Terminology	Theoretical Description	References
Entropy (<i>ENT</i>)	Detects the randomness of grey level distribution. Entropy will be higher for nearly random or noisy images.	[59]
Angular second moment (<i>ASM</i>)	Detects disorder in texture. High energy values represent the constant of periodic form of gray level distribution	[53,60]
Contrast (<i>CON</i>)	The difference between the highest and the lowest values of a connecting set of pixels. Contrast is greater for images that have rapidly fluctuating intensities.	[61]
GLCM variance (<i>VAR</i>)	The degree of heterogeneity. Variance increases when the gray level values differ from their mean.	[62]
Correlation (<i>COR</i>)	Measures linear-dependencies of gray tone in the image.	[63]
Homogeneity (<i>HOM</i>)	Gives maximum value when all elements in the image are same.	[49]
Dissimilarity (<i>DIS</i>)	Assists to distinguish most surface features.	[64]
GLCM Mean (<i>MEAN</i>)	Measures the mean of Grey level co-occurrences values. Generally least correlated with other texture parameters.	[65]

2.3.4. Regression Model Development

Multivariate linear regression was employed to generate combined backscatter, polarimetric parameter, and texture-based models to predict f_p . Spearman's rank correlation analysis was used to assess correlation between parameters and with f_p while accounting for any non-normal distributions. A coefficient threshold of 0.7 was used to identify multicollinearity between parameters. Correlated parameter pairs were assessed against f_p , and the parameter with the higher correlation with f_p was kept for regression model development. Model selection was then accomplished using forward stepwise regression analysis with an entry p -value of 0.05. These analyses were performed separately for the three θ ranges (NR, MR and FR). Therefore, a different model is derived for each of the three θ ranges.

To identify any misspecifications in the multivariate regression models, and to support the accuracy values obtained with multivariate regression, a random forest regression [66] was also performed, using the random Forest package in the statistical package-R. The number of parameters used at each split was set to the number of parameters divided by 3, and 500 trees were used.

The reduced parameter set, following removals due to correlation, was used for the random forest regression as well, since multicollinearity has been found to be detrimental [67].

Model accuracy was evaluated via RMSE analysis of predicted f_p values versus observed values in the test set. This was done for both multivariate and random forest regressions. Multivariate regression models were used to estimate f_p for RS-2 SAR scenes resampled to coarser 750 m by 750 m pixels to match the scale of the input sample data. To examine whether model estimates are sensitive to scale, images were also resampled to 500 m and 250 m pixel spacings.

2.3.5. Snow Thickness Images

Given the association of f_p and winter snow thickness [7,8], we infer the spatial distribution of relative snow thickness based on predicted f_p . To constrain the snow thickness, we assume that our in-situ-measured range of snow thickness (1.5 cm to 40 cm) is representative of the SAR scene extents (25 km by 25 km), which encompasses the study area. We linearly categorized the in-situ-measured snow thickness into eight classes, evenly-distributed across the snow thickness range, and related them to eight f_p classes ranging from 0.25–0.85 (i.e., lowest f_p class is equivalent to the highest class of snow thickness). This provides a rudimentary hindcast of snow thickness.

3. Results and Discussion

3.1. Relationship between Winter SAR Backscatter and Pond Fraction

Spearman rank correlation coefficients between RS-2 parameters and f_p are shown in Table 4. σ_{HH}^0 is correlated with one or more parameters in each θ range and is thus not included in model development; it is shown in Table 4 for comparison. In the NR, σ_{HV}^0 and $MEAN_{R_{VVHH}}$ exceed 0.5, as does σ_{HH}^0 . The value for σ_{HV}^0 (−0.652) is within the range reported in Scharien et al. [24] (−0.647 to −0.792), but the value for σ_{HH}^0 (−0.540) is slightly lower than their range (−0.590 to −0.824). Our relatively higher correlation value for σ_{HV}^0 may relate to the lower noise floor of our data; suggesting that σ_{HV}^0 was limited by the noise floor in Scharien et al. [24]. Our study examines data at a much lower noise floor: −37 dB (NR) to −33 dB (FR) for RS-2 fine quad-polarization mode (MDA, 2014), versus −20 dB to −22 dB for Envisat-ASAR and Sentinel-1 [68,69]. For σ_{HV}^0 , our mean backscatter exceeds the RS-2 fine quad-polarization noise floor by 6.4 dB at NR, by 4.0 dB at MR, and by 3.1 dB at FR. In the MR, three parameters exceed 0.5: $MEAN_{HV}$, $MEAN_{HH}$ and ASM_{HV} , plus σ_{HH}^0 . Our correlation for σ_{HH}^0 (−0.552) is lower than the range reported by Scharien et al. [24] (−0.695 to −0.810). However, our lower noise floor is likely the cause of our texture parameters derived from σ_{HV}^0 exhibiting relatively strong correlation with f_p at MR when using RS-2, whereas the noise floor was found to be a limiting factor in Scharien et al. [24]. In the FR, three parameters exceed 0.5: σ_{VV}^0 , VAR_{VV} and $MEAN_A$, plus σ_{HH}^0 . We find σ_{VV}^0 to consistently have higher correlation with f_p than σ_{HH}^0 , suggesting that employing σ_{VV}^0 instead of σ_{HH}^0 may improve the results of Scharien et al. [24]. Overall, our correlation values are not as high as those found by Scharien et al. [24], which may be the result of their object-based approach versus our polygon-based approach. In comparison to Fors et al. [23], we find higher correlations for H , α , ρ and ϕ at FR, but lower correlations for H , α , ρ and ϕ at NR. Given that their X-band correlations are for sea ice with existing melt ponds, versus our C-band correlations for snow covered sea ice during winter, discrepancies are not unexpected.

The correlation analysis reveals multicollinearity between many parameters ($r \geq 0.7$). Of the original 81 parameters, 64 are correlated at NR, 57 at MR and 62 at FR; the remaining less-correlated parameters are used for model development; these are shown in Table 4.

Given that late winter σ_{VV}^0 and σ_{HV}^0 exhibit negative correlation with melt season f_p (Table 4; e.g., Figures 4 and 5), and that f_p is inversely correlated with late winter snow thickness [7], we infer that σ_{VV}^0 , and σ_{HV}^0 increase with snow thickness in a manner similar to previous studies [2,39]. R_{VVHH} exhibits substantial negative correlation with f_p at MR (e.g., Figure 6). R_{VVHH} pixel values are primarily negative, indicating that $\sigma_{HH}^0 > \sigma_{VV}^0$, suggesting that Fresnel reflection effects associated with a smooth

dielectric interface are responsible [70]. R_{VVHH} tends toward 0 dB as f_p decreases, pointing to reduced Fresnel reflection, which, in turn, may be associated with rougher FYI and thicker snow.

Table 4. Parameters used for model development. Parameters have low correlation with each other (Spearman’s $r < 0.7$). Parameters are shown in descending order of absolute correlation (Spearman’s) with f_p . NR = near-range, MR = mid-range, and FR = far-range incidence angles. σ_{HH}^0 (value in italics) is included for comparison.

NR Parameters	r	MR Parameters	r	FR Parameters	r
σ_{HV}^0	-0.652	$MEAN_{HV}$	-0.627	σ_{VV}^0	-0.584
σ_{HH}^0	-0.540	$MEAN_{HH}$	-0.579	$MEAN_A$	-0.550
$MEAN_{R_{VVHH}}$	-0.532	σ_{HH}^0	-0.552	σ_{HH}^0	-0.540
COR_A	0.473	ASM_{HV}	0.500	VAR_{VV}	-0.501
$COR_{R_{VVHH}}$	-0.336	R_{VVHH}	-0.497	$MEAN_\phi$	-0.464
HOM_{HH}	-0.323	COR_{HV}	-0.427	HOM_{HV}	0.440
ENT_{HH}	0.304	VAR_{VV}	-0.361	H	0.382
$MEAN_{VV}$	-0.285	$MEAN_\phi$	-0.351	HOM_{VV}	0.364
$VAR_{R_{VVHH}}$	-0.271	$MEAN_{R_{VVHH}}$	-0.344	R_{VVHH}	-0.312
COR_{VV}	-0.253	A	-0.299	ASM_ρ	-0.293
COR_α	-0.224	ϕ	-0.285	HOM_α	-0.211
COR_ϕ	-0.196	VAR_{HH}	-0.259	COR_A	-0.156
COR_ρ	-0.177	$MEAN_A$	-0.242	ASM_A	-0.116
HOM_{HV}	0.164	VAR_A	-0.241	VAR_A	-0.105
HOM_ρ	-0.135	VAR_ϕ	-0.229	HOM_H	-0.072
$MEAN_\phi$	0.080	COR_α	-0.206	DIS_H	0.066
α	0.065	COR_{HH}	-0.180	ASM_H	-0.058
		$VAR_{R_{VVHH}}$	-0.164	CON_A	-0.052
		ASM_ϕ	0.154	HOM_A	-0.04
		ASM_{VV}	0.152		
		$ASM_{R_{VVHH}}$	0.113		
		COR_ϕ	-0.105		
		ASM_{HH}	0.073		
		α	-0.050		
		ρ	0.042		

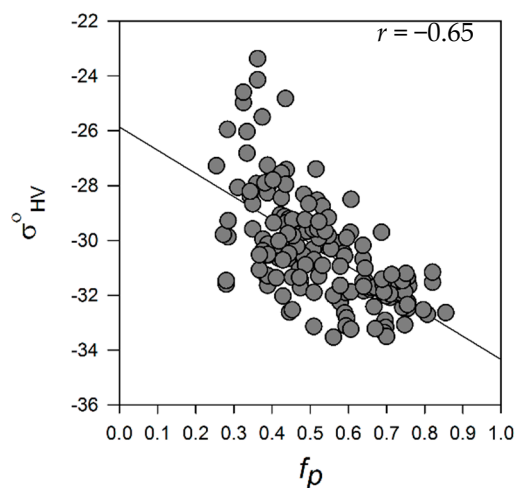


Figure 4. Late winter σ_{HV}^0 (dB) as a function of f_p at NR. The solid line represents the linear dependency, and r is the Spearman correlation.

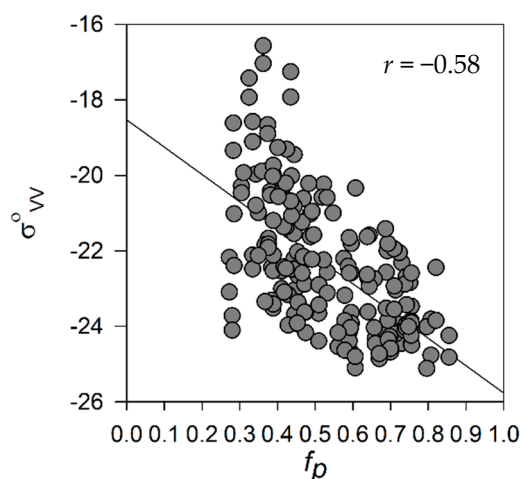


Figure 5. Late winter σ_{VV}^0 (dB) as a function of f_p at FR. The solid line represents the linear dependency, and r is the Spearman correlation.

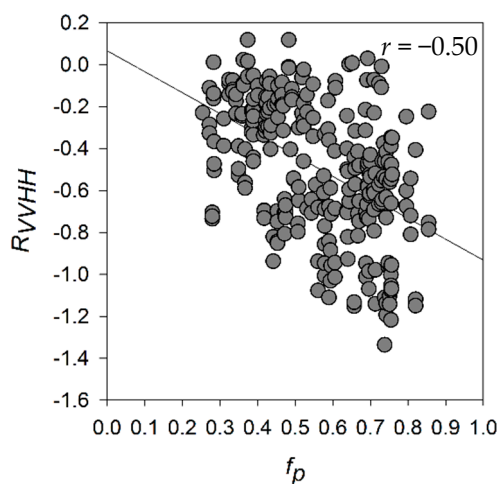


Figure 6. Late winter R_{VVHH} (dB) as a function of f_p at MR. The solid line represents the linear dependency, and r is the Spearman correlation.

Texture parameters most correlated with f_p are primarily based on σ_{HV}^0 , σ_{VV}^0 , σ_{HH}^0 , R_{VVHH} , ϕ and A (Table 4, Figures 7–9). Texture parameters that are correlated with f_p and derived from σ_{HV}^0 are present in all three θ ranges. Their correlation with f_p suggests that σ_{HV}^0 might be sensitive to different snow thicknesses as well. σ_{HV}^0 is influenced by surface roughness, volume scattering and multi-bounce scattering [71]; as snow thickness increases, the potential for increased volume scattering increases [72]. Thicker snow covers are associated with rougher sea ice [9], which may also influence σ_{HV}^0 because cross polarization is the result of multiple volume scattering enhanced by the presence of uneven surfaces [73]. Therefore, it is not surprising that texture parameters associated with σ_{HV}^0 are sensitive to ice and snow surface structure and related melt season f_p . Texture parameters based on ϕ and A are present in all three θ ranges, suggesting that these parameters may be sensitive to snow thickness differences and are therefore correlated with f_p .

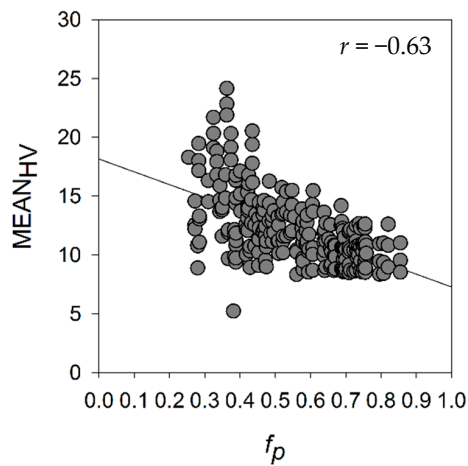


Figure 7. Late winter $MEAN_{HV}$, as a function of f_p at MR. The solid line represents the linear dependency, and r is the Spearman correlation.

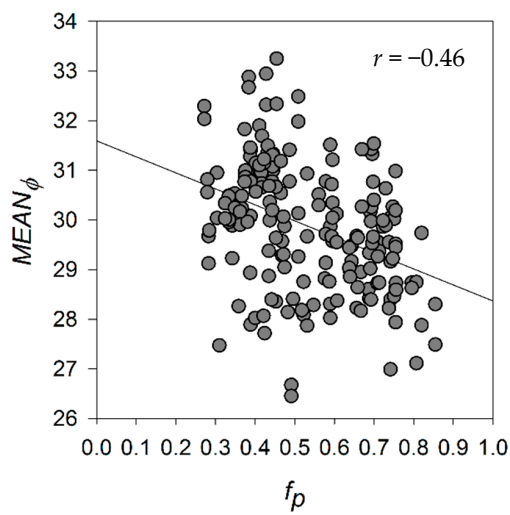


Figure 8. Late winter $MEAN_{\phi}$, as a function of f_p at FR. The solid line represents the linear dependency, and r is the Spearman correlation.

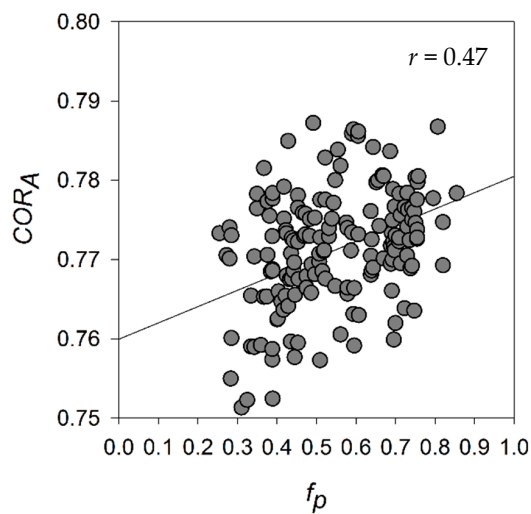


Figure 9. Late winter COR_A , as a function of f_p at NR. The solid line represents the linear dependency, and r is the Spearman correlation.

3.2. Prediction of Pond Fraction

The regression analysis produced the following models for predicting f_p at NR, MR and FR, respectively:

$$f_{p(NR)} = 0.897 - 0.048\sigma_{HV}^0 + 0.726ENT_{HH} - 0.059MEAN_{\phi} - 2.939COR_{\alpha} + 0.020\alpha \quad (3)$$

$$f_{p(MR)} = 2.912 - 0.022MEAN_{HV} - 0.052MEAN_{\phi} - 0.012MEAN_A - 0.787COR_{HV} - 0.094R_{VVHH} \quad (4)$$

$$f_{p(FR)} = 2.227 - 0.015\sigma_{VV}^0 - 0.059MEAN_{\phi} + 2.837ASM_H - 0.015MEAN_A - 0.174VAR_{VV} \quad (5)$$

The models, as represented by Equations (3)–(5), exhibit R^2 values of 0.57, 0.61, and 0.62 respectively. The FR model exhibits the highest R^2 and contains a linear parameter and four texture parameters. The MR model exhibits the second highest R^2 and contains one linear parameter and four texture parameters. All models make use of polarimetric data for the contributing texture parameters. The robustness of the models is consistent with previous findings in that the inclusion of texture with linear and/or polarimetric parameters improves classification results [48–51].

Differing scattering mechanisms at NR, MR and FR are very likely responsible for the three different models. Surface roughness changes depending on the local θ [74]; surface scattering dominates at NR, and volume scattering dominates at FR [41,43]. In addition, the polarimetric parameters that were found to have low correlation with other parameters are likely sensitive to specific scattering mechanisms; this may explain their inclusion in the models even if their correlation with f_p is low (Table 4). In comparison to the models developed by Scharien et al. [24], the model parameters here suggest that the addition of polarimetric capabilities can be a benefit, and a lower noise floor is a benefit when using HV. However, the use of additional model parameters may lead to over-fitting.

Random forest regression analysis provides predictive ability similar to the linear regression (see Section 3.3). An assessment of random forest parameter importance supports the parameter selection in the linear regression models (Table 5); most of the linear regression parameters are found in the top five important positions. Differences between models are expected due to their different selection techniques. Give the random forest results, no gross misspecification is anticipated in the linear models.

Table 5. Random forest regression parameters in order of parameter importance (increase in mean-squared-error with removal (IncMSE)), for NR, MR and FR models. The top 13 important positions are shown. Shaded parameters are found in the respective linear regression models.

NR	IncMSE	MR	IncMSE	FR	IncMSE
σ_{HV}^0	0.0116	$MEAN_{HV}$	0.0058	$MEAN_{\phi}$	0.0046
$MEAN_{R_{VVHH}}$	0.0036	ASM_{HV}	0.0038	$MEAN_A$	0.0039
$MEAN_{VV}$	0.0015	$MEAN_{HH}$	0.0036	σ_{VV}^0	0.0035
ENT_{HH}	0.0010	R_{VVHH}	0.0029	HOM_{VV}	0.0021
COR_{α}	0.0010	$MEAN_A$	0.0021	VAR_{VV}	0.0018
HOM_{HH}	0.0009	A	0.0021	HOM_{HV}	0.0017
COR_A	0.0009	$MEAN_{\phi}$	0.0017	R_{VVHH}	0.0008
α	0.0005	ϕ	0.0013	COR_A	0.0007
COR_{VV}	0.0004	COR_{HV}	0.0012	H	0.0006
$VAR_{R_{VVHH}}$	0.0004	VAR_A	0.0008	ASM_p	0.0003
$MEAN_{\phi}$	0.0004	VAR_{VV}	0.0007	ASM_H	0.0002
HOM_p	0.0003	$VAR_{R_{VVHH}}$	0.0006	ASM_A	0.0002
HOM_{HV}	0.0002	$ASM_{R_{VVHH}}$	0.0005	HOM_A	0.0002

3.3. Error Analysis

Predicted f_p , using Equations (3)–(5), is compared with measured f_p for the 325 test samples, for each θ range (Figure 10). The RMSE was found to be 0.106 for NR, 0.108 for MR, and 0.094 for FR.

The RMSE values obtained with random forest regression are 0.109, 0.091 and 0.092, for NR, MR and FR models, respectively. The NR linear model exhibits greater skill than the random forest model; however, the MR linear model is substantially worse than for random forest. Nevertheless, these values indicate that the multivariate linear regression models have predictive capabilities similar to that of random forest models and can thus be used without significant loss of skill.

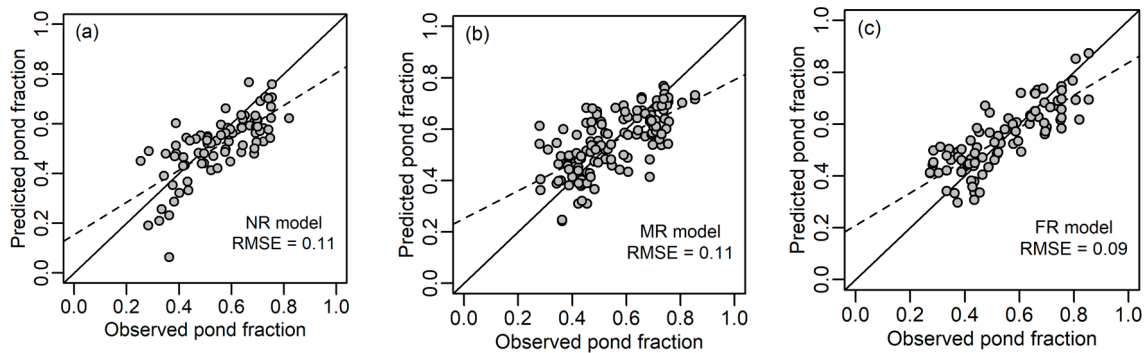


Figure 10. Observed (estimated via aerial photography) and regression model predicted f_p at (a) NR, (b) MR and (c) FR. The dashed line is the linear dependency of the comparison. The solid line represents the 1:1 relationship.

It is apparent that the models overestimate lower f_p and underestimate higher f_p Figure 10. The underestimation of higher f_p is most pronounced at MR (Figure 10b). However, the linear dependencies are consistent across the three θ ranges.

3.4. SAR Scene Pond Fraction Estimates

The NR, MR and FR f_p prediction models are applied to late winter SAR scenes with pixel spacing of 750 m, 500 m and 250 m to assess the dependency of pixel size (Figures 11–13). The areas represented by the models at lower and higher resolution indicate similar pattern and variability, indicating that the models are appropriate at higher resolution. The higher resolution SAR scene displays higher variability than the 750 m or 500 m scenes, which is logical as 250 m pixel spacing would reveal more detail. There are possible mixed-pixel effects where sea ice abuts land because the land mask used may not be perfectly accurate in all cases. However, these effects only impact the sea ice pixels immediately adjacent to the coastlines. Buffering the coastline would mitigate this issue, if needed.

Within the area of overlapping scenes (red outline in Figure 11a), some differences in the estimates can be observed. In general, the NR estimates (Figure 11) exhibit lower pond fractions than do the MR (Figure 12) and FR (Figure 13) estimates; especially at the north end of Griffith Island and associated with the linear feature extending from Sheringham Point. The latter is a region of rougher, ridged, sea ice which is expected to have thicker snow cover and smaller f_p . The efficacy of the NR model to show such smaller f_p is supported by the error analysis which shows that NR exhibits somewhat less bias at small f_p (Figure 10a). Conversely, the FR estimates show larger areas of higher f_p than MR and NR. This is also supported by the error analysis, which shows a smaller bias at high f_p for FR (Figure 10c). The MR estimates appear to lack the range of f_p , compared to the NR and FR estimates; this is also displayed in the error analysis (Figure 10b). Given these observations, it may be beneficial to make use of combined NR and FR estimates. The estimates of f_p with regard to incidence angle are very likely a function of the different scattering mechanisms that dominate at the respective incidence angle ranges and the sensitivity of the different parameter combinations in the models to these scattering mechanisms.

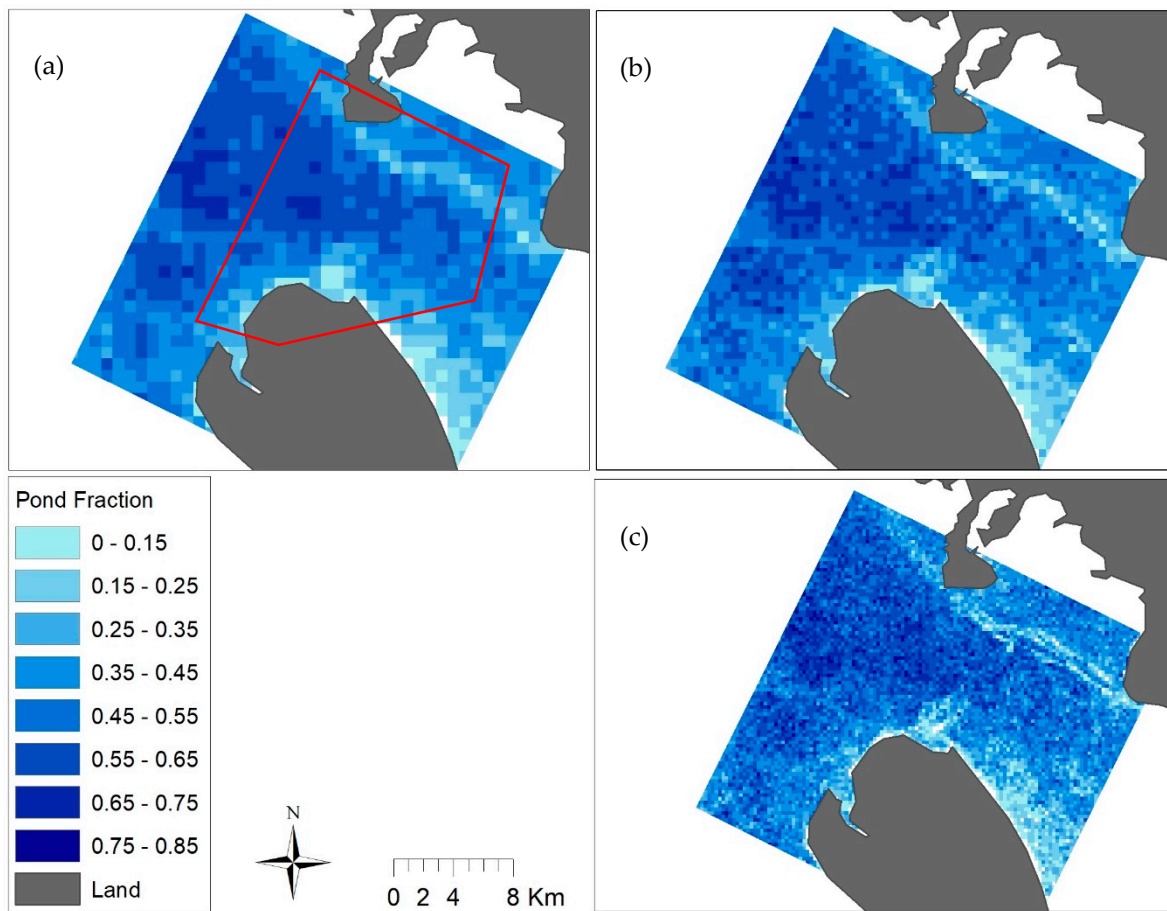


Figure 11. Predicted melt f_p at 750 m (a), 500 m (b) and 250 m (c) pixel spacing, respectively, at NR. Based on RS-2 FQ4 2012-05-10 data. The red outline in (a) delineates the area where the NR, MR and FR scenes overlap.

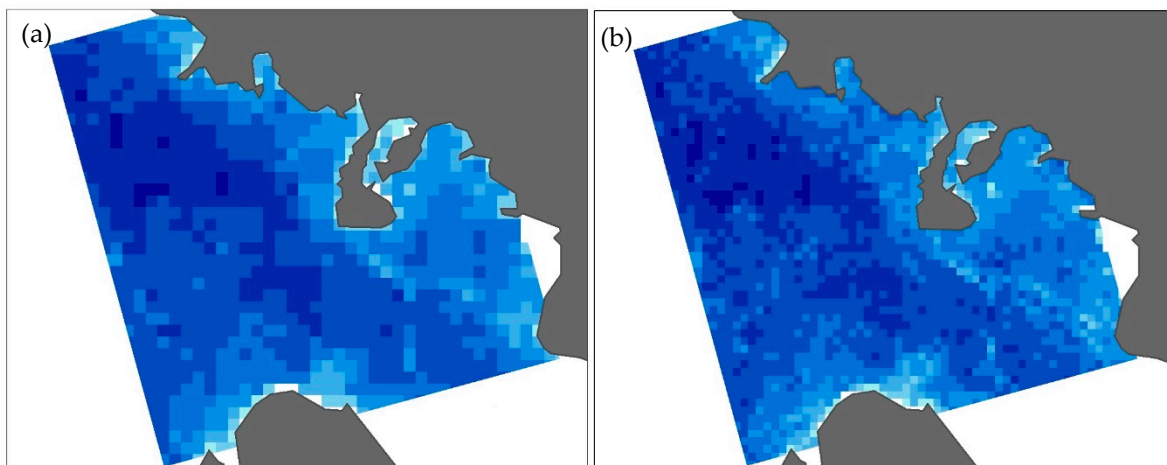


Figure 12. Cont.

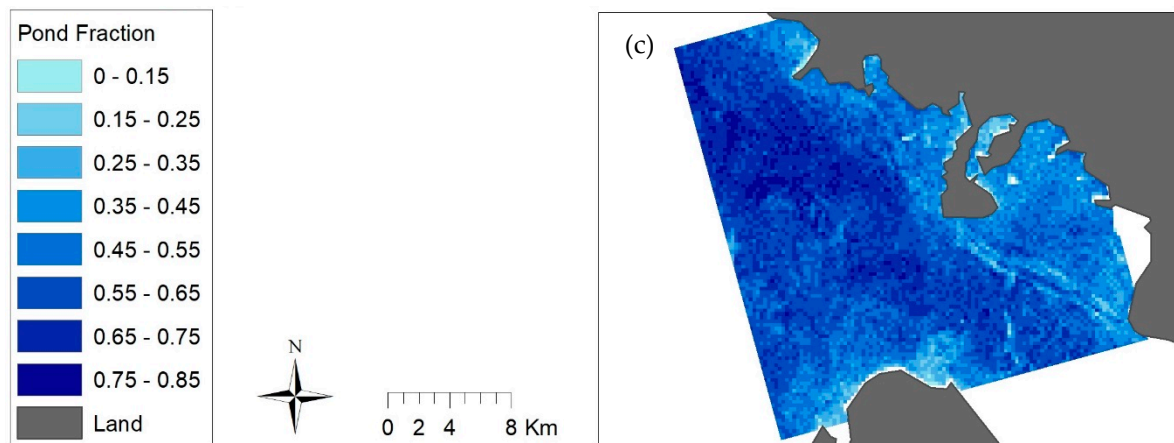


Figure 12. Predicted melt f_p at 750 m (a), 500 m (b) and 250 m (c) pixel spacing, respectively, at MR. Based on RS-2 FQ15 2012-05-21 data.

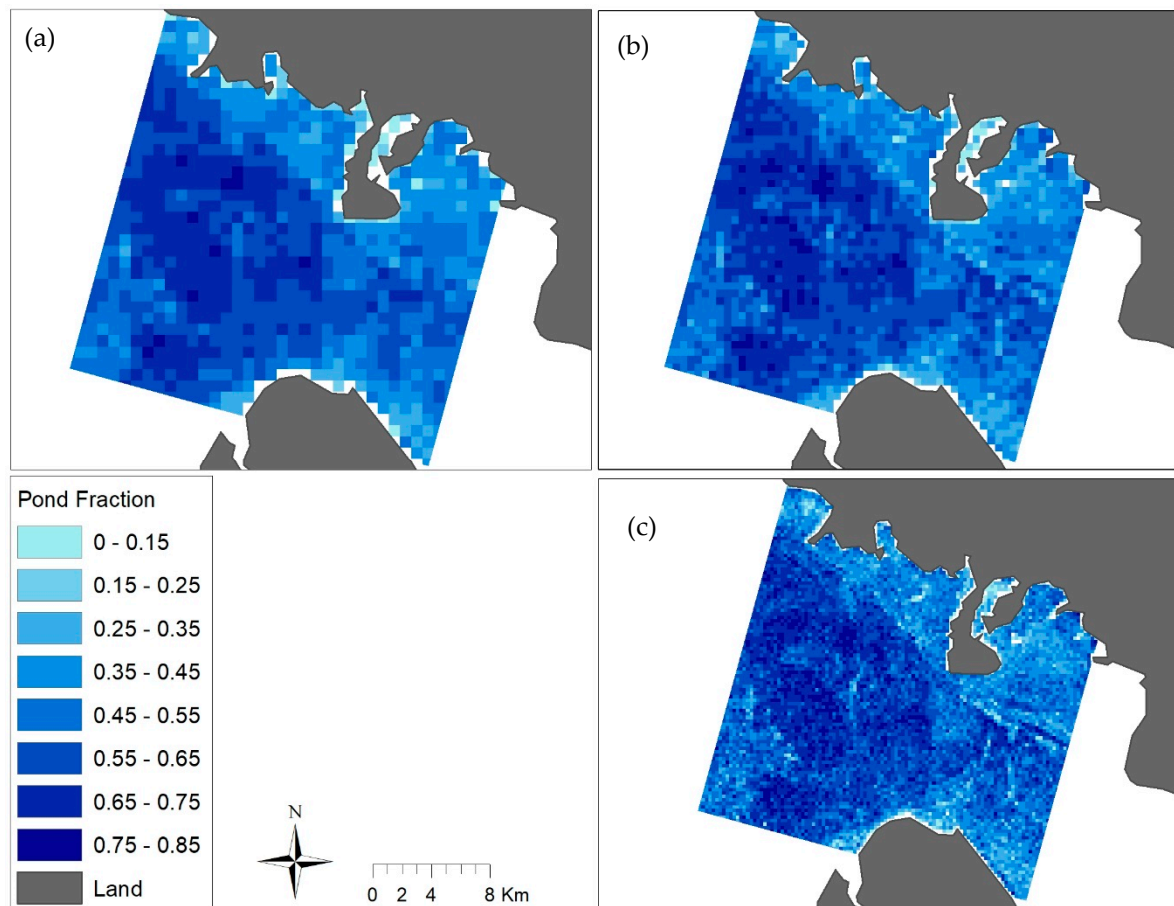


Figure 13. Predicted melt f_p at 750 m (a), 500 m (b) and 250 m (c) pixel spacing, respectively, at FR. Based on RS-2 FQ23 2012-05-15 data.

3.5. SAR-Based Estimation of Snow Thickness

The snow thickness of our in-situ sample site ranges from 1.5 cm to 40 cm, with a mean thickness of $10.9 \text{ cm} \pm 7.7 \text{ cm}$ (Figure 2). This range of snow thickness is representative of FYI in the Canadian Arctic Archipelago; however, the mean snow thickness is lower than values previously found for relatively smooth FYI [75]. Considering the range of snow thickness in our study area, first-order hindcasts of snow thickness distribution were generated (Figures 14–16) based on the association of snow thickness

and f_p . The prediction maps provide insight into the snow thickness distribution within a 25 km by 25 km SAR scene. Of note is the higher accumulation of snow near the coastlines. This is because during wind drift, the uneven land surface topography causes more snow to accumulate on the leeward side [76] than in the homogeneous and smooth areas of FYI. The models illustrate a similar pattern of snow thickness distribution and show snow thickness variability at both fine and coarser resolution. Snow accumulation also depends on ice deformation [77], with snow catchment higher in deformed ice areas compared to smooth ice surfaces. The model hindcast maps indicating appreciably higher snow thickness along linear features near to the Cornwallis Island coastline appear to be reasonably well associated with the spatial location of narrow sea ice ridges as observed in the winter SAR imagery. Most of the study area exhibits a thin snow cover consistent with a relatively smooth surface. At both 750 m and 250 m pixel spacing, the models show similar pattern and variability of snow thickness.

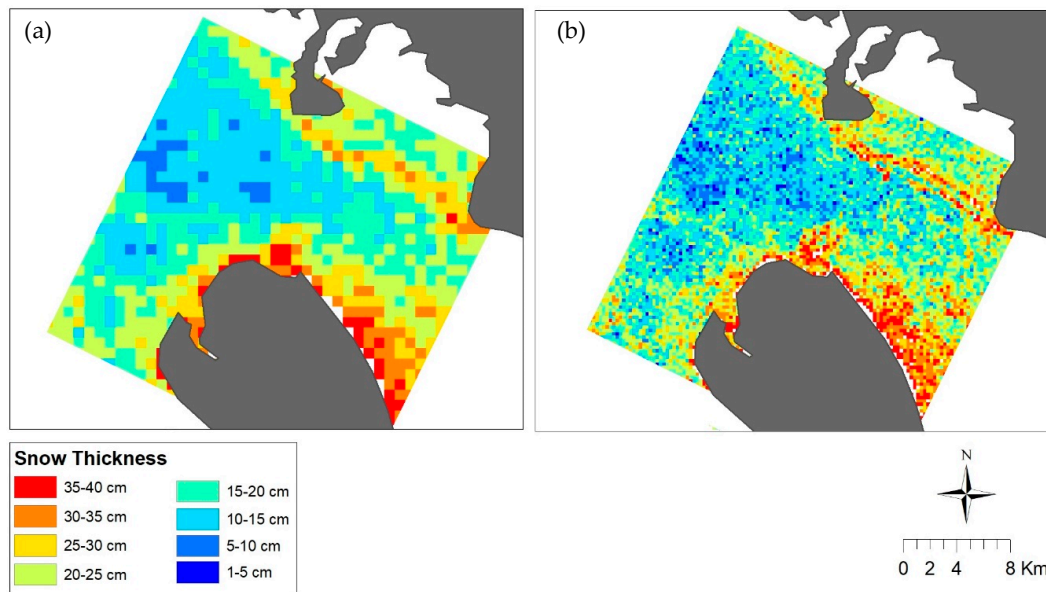


Figure 14. Snow thickness class spatial distribution from the NR model at 750 m (a) and 250 m (b) pixel spacing. Grey area represents land. Based on RS-2 FQ4 2012-05-10 data.

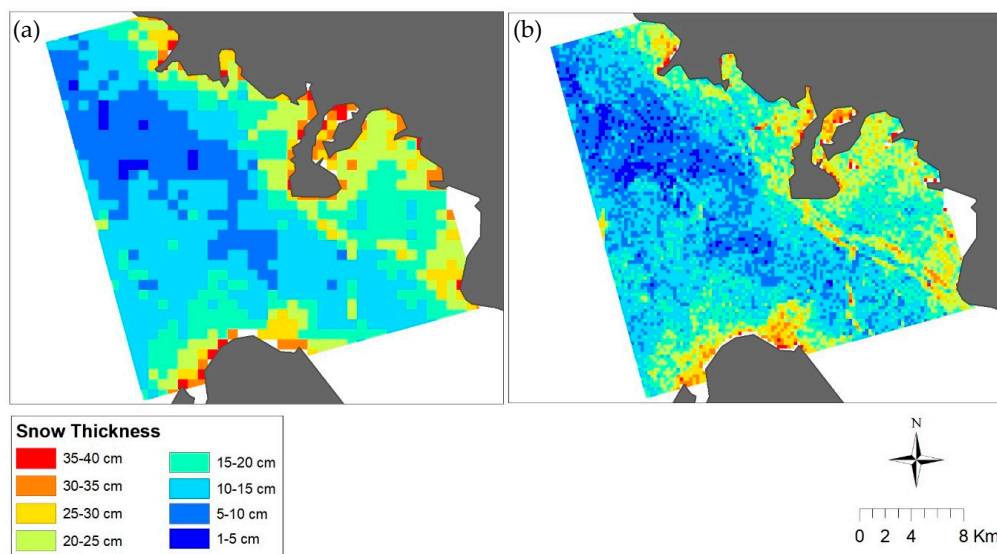


Figure 15. Snow thickness class spatial distribution from the MR model at 750 m (a), and 250 m (b) pixel spacing, respectively. Grey area represents land. Based on RS-2 FQ15 2012-05-21 data.

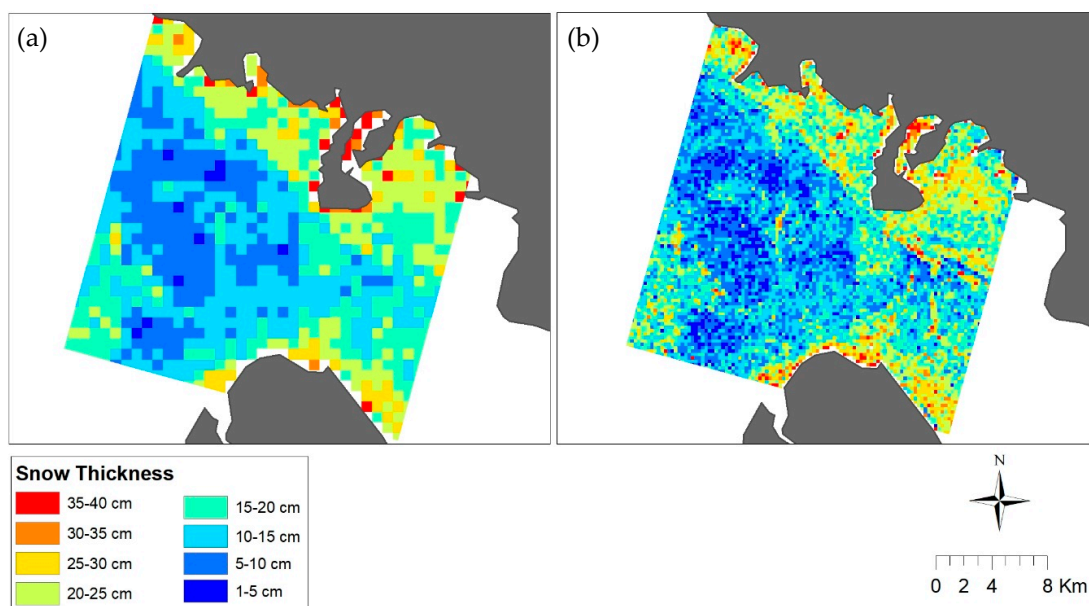


Figure 16. Snow thickness class spatial distribution from the FR model at 750 m (a) and 250 m (b) pixel spacing. Grey area represents land. Based on RS-2 FQ23 2012-05-15 data.

Between the NR, MR and FR snow thickness estimates, NR (Figure 14) exhibits the greatest snow depths. This relates directly to the smaller f_p estimates with the NR model as discussed in the previous section. The reduced bias at small f_p with NR (Figure 10a) likely provides the best estimates of thick snow. Thinner snow estimates appear to have the most realistic spatial distribution at FR (Figure 16). Again, this relates directly to the smaller bias at large f_p with FR (Figure 10c), where thinner snow is expected.

4. Conclusions

This paper presents an approach utilizing late winter C-band RADARSAT-2 SAR linear, polarimetric and texture parameters of snow covered first-year sea ice to predict early summer melt pond fraction. Predictions were then used to examine relationships between early melt pond fraction and late winter snow thickness. We estimated melt pond fractions from the aerial photographs collected over first-year sea ice. The correlation of melt pond fraction and late winter backscatter parameters provided us with the ability to hindcast snow thickness. Nine linear and polarimetric parameters and 72 texture parameters were evaluated for their relationship with pond fraction.

Multivariate models comprised of linear, polarimetric and/or texture parameters are derived at near-, mid- and far-range incidence angles. The best pond fraction prediction capability is exhibited by the model at far-range incidence angles ($RMSE = 0.09$).

By relating late winter snow thickness and f_p , these predictions help us to understand the winter snow thickness variability. The models are able to distinguish higher snow thickness along sea ice ridges, coastlines and relatively thinner snow cover on smooth surfaces of first-year sea ice, which is consistent with previous findings.

Moreover, the models show that the combination of SAR linear and polarimetric backscatter and texture parameters enhance the strength of the models compared to utilizing them separately for the prediction of pond fraction. The estimation of pond fraction over an entire SAR scene based on the models show logical distributions of melt ponds and snow thickness.

The results of this study add to the suite of seasonal sea ice forecasting tools, and thus can aid ship navigability since melt ponds are associated with advanced sea ice melt and significant weakening of sea ice mechanical strength. At the same time, it provides insight into the late winter snow thickness distribution on first year sea ice. The method is tested on landfast sea ice, is sensitive to the time

periods of the collected aerial melt pond distributions and SAR scene acquisitions, and is likely not applicable to drift ice. Future research should test this model on a regional scale, and similar models should also be evaluated for their application over multi-year sea ice and more deformed types of first-year sea ice.

Author Contributions: S.R., T.G. and J.Y. designed the experiment. S.R. formulated the research methodology and wrote the manuscript. R.S. provided necessary data and contributed to manuscript development and proof reading. T.G. and J.Y. contributed with additional inputs during manuscript development and proof reading.

Funding: This research was funded by Canadian NSERC Discovery grants to John Yackel and Randy Scharien as well as MEOPAR (Marine Environmental Observation Prediction and Response Network) funding to Randy Scharien. The APC was funded by Canadian NSERC Discovery grants to John Yackel.

Acknowledgments: The authors would like to thank the participants of the Arctic-ICE 2012 Field Experiment based out of Resolute Bay, Nunavut, Canada. We would like to thank all team members for their support and hard work in the field program, including Principal Investigators, C.J. Mundy (CEOS, University of Manitoba) and B. Else (University of Calgary). We highly appreciate M.M. Rahman (University of Calgary) for his assistance in GLCM texture analysis. The authors would like to thank for the valuable comments provided by the reviewers; their contributions have substantially improved this paper. We also appreciate the collegial assistance from M. Mahmud and V. Nandan. We extend our sincere thanks to the Polar Continental Shelf Project and MEOPAR (Marine Environmental Observation Prediction and Response Network) for their funding and logistical support. We acknowledge Canadian NSERC Discovery grants to R. Scharien and J. Yackel towards this work. The Canadian Ice Service support in providing, planning and ordering RADARSAT-2 imagery is appreciated. Supplementary RADARSAT-2 imagery and planning support was provided by the Canadian Space Agency's Science and Operational Applications Research program. RADARSAT-2 Data and Products © MacDonald, Dettwiler and Associates Ltd. 2012. All Rights Reserved. RADARSAT is an official mark of the Canadian Space Agency.

Conflicts of Interest: The authors declare no conflict of interest.

References

- Holt, B.; Digby, S.A. Processes and imagery of first-year fast sea ice during the melt season. *J. Geophys. Res. Oceans* **1985**, *90*, 5045–5062. [[CrossRef](#)]
- Barber, D.G.; Nghiem, S.V. The role of snow on the thermal dependence of microwave backscatter over sea ice. *J. Geophys. Res. Oceans* **1999**, *104*, 25789–25803.
- Yackel, J.J.; Barber, D.G.; Hanesiak, J.M. Melt ponds on sea ice in the Canadian Archipelago. I—Variability in morphological and radiative properties. *J. Geophys. Res.* **2000**, *105*, 22049–22060. [[CrossRef](#)]
- Scharien, R.K.; Yackel, J.J. Analysis of surface roughness and morphology of first-year sea ice melt ponds: Implications for microwave scattering. *IEEE Trans. Geosci. Remote Sens.* **2005**, *43*, 2927–2939. [[CrossRef](#)]
- Iacozza, J.; Barber, D.G. Ablation patterns of snow cover over smooth first-year sea ice in the Canadian Arctic. *Hydrol. Process.* **2001**, *15*, 3559–3569. [[CrossRef](#)]
- Eicken, H.; Krouse, H.R.; Kadko, D.; Perovich, D.K. Tracer studies of pathways and rates of meltwater transport through Arctic summer sea ice. *J. Geophys. Res. Oceans* **2002**, *107*. [[CrossRef](#)]
- Yackel, J.J.; Barber, D.G.; Papakyriakou, T.N.; Breneman, C. First-year Sea ice spring melt transitions in the Canadian Arctic Archipelago from time-series synthetic aperture radar data, 1992–2002. *Hydrol. Process.* **2007**, *21*, 253–265. [[CrossRef](#)]
- Polashenski, C.; Perovich, D.; Courville, Z. The mechanisms of sea ice melt pond formation and evolution. *J. Geophys. Res. Oceans* **2012**, *117*. [[CrossRef](#)]
- Iacozza, J.; Barber, D.G. An examination of snow redistribution over smooth land-fast sea ice. *Hydrol. Process.* **2010**, *24*, 850–865. [[CrossRef](#)]
- Iacozza, J.; Barber, D.G. An examination of the distribution of snow on sea-ice. *Atmos. Ocean* **1999**, *37*, 21–51.
- Webster, M.A.; Rigor, I.G.; Perovich, D.K.; Richter-Menge, J.A.; Polashenski, C.M.; Light, B. Seasonal evolution of melt ponds on Arctic sea ice. *J. Geophys. Res. Oceans* **2015**, *120*, 5968–5982. [[CrossRef](#)]
- Landy, J.; Ehn, J.; Shields, M.; Barber, D. Surface and melt pond evolution on landfast first-year sea ice in the Canadian Arctic Archipelago. *J. Geophys. Res. Oceans* **2014**, *119*, 3054–3075. [[CrossRef](#)]
- Markus, T.; Cavalieri, D.J.; Tschudi, M.A.; Ivanoff, A. Comparison of aerial video and Landsat 7 data over ponded sea ice. *Remote Sens. Environ.* **2003**, *86*, 458–469. [[CrossRef](#)]
- Tschudi, M.A.; Maslanik, J.A.; Perovich, D.K. Derivation of melt pond coverage on Arctic sea ice using MODIS observations. *Remote Sens. Environ.* **2008**, *112*, 2605–2614. [[CrossRef](#)]

15. Rösel, A.; Kaleschke, L.; Birnbaum, G. Melt ponds on Arctic sea ice determined from MODIS satellite data using an artificial neural network. *Cryosphere* **2012**, *6*, 431–446. [[CrossRef](#)]
16. Zege, E.; Malinka, A.; Katsev, I.; Prikhach, A.; Heygster, G.; Istomina, L.; Schwarz, P. Algorithm to retrieve the melt pond fraction and the spectral albedo of Arctic summer ice from satellite optical data. *Remote Sens. Environ.* **2015**, *163*, 153–164. [[CrossRef](#)]
17. Istomina, L.; Heygster, G.; Huntemann, M.; Schwarz, P.; Birnbaum, G.; Scharien, R.; Polashenski, C.; Perovich, D.; Zege, E.; Malinka, A.; et al. Melt pond fraction and spectral sea ice albedo retrieval from MERIS data—Part 1: Validation against in situ, aerial, and ship cruise data. *Cryosphere* **2015**, *9*, 1551–1566. [[CrossRef](#)]
18. Istomina, L.; Heygster, G.; Huntemann, M.; Marks, H.; Melsheimer, C.; Zege, E.; Malinka, A.; Prikhach, A.; Katsev, I. Melt pond fraction and spectral sea ice albedo retrieval from MERIS data—Part 2: Case studies and trends of sea ice albedo and melt ponds in the Arctic for years 2002–2011. *Cryosphere* **2015**, *9*, 1567–1578. [[CrossRef](#)]
19. Tanaka, Y.; Tateyama, K.; Kameda, T.; Hutchings, J.K. Estimation of melt pond fraction over high-concentration Arctic sea ice using AMSR-E passive microwave data. *J. Geophys. Res. Oceans* **2016**, *121*, 7056–7072. [[CrossRef](#)]
20. Barber, D.G.; Yackel, J. The physical, radiative and microwave scattering characteristics of melt ponds on Arctic landfast sea ice. *Int. J. Remote Sens.* **1999**, *20*, 2069–2090. [[CrossRef](#)]
21. Mäkynen, M.; Kern, S.; Rösel, A.; Pedersen, L.T. On the estimation of melt pond fraction on the Arctic Sea ice with ENVISAT WSM images. *IEEE Trans. Geosci. Remote Sens.* **2014**, *52*, 7366–7379. [[CrossRef](#)]
22. Scharien, R.K.; Landy, J.; Barber, D.G. First-year sea ice melt pond fraction estimation from dual-polarisation C-band SAR—Part 1: In situ observations. *Cryosphere* **2014**, *8*, 2147–2162. [[CrossRef](#)]
23. Fors, A.S.; Divine, D.V.; Doulgeris, A.P.; Renner, A.H.; Gerland, S. Signature of Arctic first-year ice melt pond fraction in X-band SAR imagery. *Cryosphere* **2017**, *11*, 755–771. [[CrossRef](#)]
24. Scharien, R.K.; Segal, R.; Nasonova, S.; Nandan, V.; Howell, S.E.; Haas, C. Winter Sentinel-1 backscatter as a predictor of spring Arctic sea ice melt pond fraction. *Geophys. Res. Lett.* **2017**, *44*. [[CrossRef](#)]
25. Scharien, R.; Segal, R.; Yackel, J.; Howell, S.; Nasonova, S. Linking winter and spring thermodynamic sea-ice states at critical scales using an object-based image analysis of Sentinel-1. *Ann. Glaciol.* **2017**, *59*, 1–15. [[CrossRef](#)]
26. Derksen, C.; Piwowar, J.; LeDrew, E. Sea-ice melt-pond fraction as determined from low level aerial photographs. *Arct. Alp. Res.* **1997**, *29*, 345–351. [[CrossRef](#)]
27. Tschudi, M.A.; Curry, J.A.; Maslanik, J.A. Determination of areal surface-feature coverage in the Beaufort Sea using aircraft video data. *Ann. Glaciol.* **1997**, *25*, 434–438. [[CrossRef](#)]
28. Barber, D.G.; Papakyriakou, T.N.; LeDrew, E.F. On the relationship between energy fluxes, dielectric properties, and microwave scattering over snow covered first-year sea ice during the spring transition period. *J. Geophys. Res. Oceans* **1994**, *99*, 22401–22411. [[CrossRef](#)]
29. Barber, D.G.; Reddan, S.P.; LeDrew, E.F. Statistical characterization of the geophysical and electrical properties of snow on landfast first-year sea ice. *J. Geophys. Res. Oceans* **1995**, *100*, 2673–2686. [[CrossRef](#)]
30. Sturm, M.; Holmgren, J.; Perovich, D.K. Winter snow cover on the sea ice of the Arctic Ocean at the Surface Heat Budget of the Arctic Ocean (SHEBA): Temporal evolution and spatial variability. *J. Geophys. Res. Oceans* **2002**, *107*. [[CrossRef](#)]
31. Bredow, J.W.; Gogineni, S. Comparison of measurements and theory for backscatter from bare and snow-covered saline ice. *IEEE Trans. Geosci. Remote Sens.* **1990**, *28*, 456–463. [[CrossRef](#)]
32. Lytle, V.I.; Jezek, K.C.; Hosseinmostafa, A.R.; Gogineni, S.P. Laboratory backscatter measurements over urea ice with a snow cover at Ku band. *IEEE Trans. Geosci. Remote Sens.* **1993**, *31*, 1009–1016. [[CrossRef](#)]
33. Markus, T.; Cavalieri, D.J. Snow depth distribution over sea ice in the Southern Ocean from satellite passive microwave data. In *Antarctic Sea Ice: Physical Processes, Interactions and Variability*; Wiley Online Library: Hoboken, NJ, USA, 1998; Volume 74, pp. 19–39.
34. Cavalieri, D.J.; Markus, T.; Ivanoff, A.; Miller, J.A.; Brucker, L.; Sturm, M.; Maslanik, J.A.; Heinrichs, J.F.; Gasiewski, A.J.; Leuschen, C.; et al. A comparison of snow depth on sea ice retrievals using airborne altimeters and an AMSR-E simulator. *IEEE Trans. Geosci. Remote Sens.* **2012**, *50*, 3027–3040. [[CrossRef](#)]
35. Maass, N.; Kaleschke, L.; Tian-Kunze, X.; Drusch, M. Snow thickness retrieval over thick Arctic sea ice using SMOS satellite data. *Cryosphere* **2013**, *7*, 1971–1989. [[CrossRef](#)]

36. Kurtz, N.T.; Farrell, S.L.; Studinger, M.; Galin, N.; Harbeck, J.P.; Lindsay, R.; Onana, V.D.; Panzer, B.; Sonntag, J.G. Sea ice thickness, freeboard, and snow depth products from Operation IceBridge airborne data. *Cryosphere* **2013**, *7*, 1035–1056. [[CrossRef](#)]
37. Kwok, R.; Kurtz, N.T.; Brucker, L.; Ivanoff, A.; Newman, T.; Farrell, S.L.; King, J.; Howell, S.; Webster, M.A.; Paden, J.; et al. Intercomparison of snow depth retrievals over Arctic sea ice from radar data acquired by Operation IceBridge. *Cryosphere* **2017**, *11*. [[CrossRef](#)]
38. Barber, D.G.; Fung, A.K.; Grenfell, T.C.; Nghiem, S.V.; Onstott, R.G.; Lytle, V.I.; Perovich, D.K.; Gow, A.J. The role of snow on microwave emission and scattering over first-year sea ice. *IEEE Trans. Geosci. Remote Sens.* **1998**, *36*, 1750–1763. [[CrossRef](#)]
39. Gill, J.P.; Yackel, J.J.; Geldsetzer, T.; Fuller, M.C. Sensitivity of C-band synthetic aperture radar polarimetric parameters to snow thickness over land fast smooth first-year sea ice. *Remote Sens. Environ.* **2015**, *166*, 34–49. [[CrossRef](#)]
40. Zheng, J.; Geldsetzer, T.; Yackel, J. Snow thickness estimation on first-year sea ice using microwave and optical remote sensing with melt modelling. *Remote Sens. Environ.* **2017**, *199*, 321–332. [[CrossRef](#)]
41. Kim, Y.S.; Onstott, R.; Moore, R. Effect of a snow cover on microwave backscatter from sea ice. *IEEE J. Ocean. Eng.* **1984**, *9*, 383–388.
42. Tjuatja, S.; Fung, A.K.; Bredow, J. A scattering model for snow-covered sea ice. *IEEE Trans. Geosci. Remote Sens.* **1992**, *30*, 804–810. [[CrossRef](#)]
43. Dierking, W.; Pettersson, M.L.; Askne, J. Multifrequency scatterometer measurements of Baltic Sea ice during EMAC-95. *Int. J. Remote Sens.* **1999**, *20*, 349–372. [[CrossRef](#)]
44. Wakabayashi, H.; Matsuoka, T.; Nakamura, K.; Nishio, F. Polarimetric characteristics of sea ice in the Sea of Okhotsk observed by airborne L-band SAR. *IEEE Trans. Geosci. Remote Sens.* **2004**, *42*, 2412–2425. [[CrossRef](#)]
45. Scheuchl, B.; Cumming, I.; Hajnsek, I. Classification of fully polarimetric single- and dual-frequency SAR data of sea ice using the Wishart statistics. *Can. J. Remote Sens.* **2005**, *31*, 61–72. [[CrossRef](#)]
46. Gill, J.P.; Yackel, J.J. Evaluation of C-band SAR polarimetric parameters for discrimination of first-year sea ice types. *Can. J. Remote Sens.* **2012**, *38*, 306–323. [[CrossRef](#)]
47. Gill, J.P.; Yackel, J.J.; Geldsetzer, T. Analysis of consistency in first-year sea ice classification potential of C-band SAR polarimetric parameters. *Can. J. Remote Sens.* **2013**, *39*, 101–117. [[CrossRef](#)]
48. Holmes, Q.A.; Nuesch, D.R.; Shuchman, R.A. Textural analysis and real-time classification of sea-ice types using digital SAR data. *IEEE Trans. Geosci. Remote Sens.* **1984**, *22*, 113–120. [[CrossRef](#)]
49. Shokr, M.E. Evaluation of second-order texture parameters for sea ice classification from radar images. *J. Geophys. Res. Oceans* **1991**, *96*, 10625–10640. [[CrossRef](#)]
50. Clausi, D.A. An analysis of co-occurrence texture statistics as a function of grey level quantization. *Can. J. Remote Sens.* **2002**, *28*, 45–62. [[CrossRef](#)]
51. Liu, H.; Guo, H.; Zhang, L. SVM-based sea ice classification using textural features and concentration from RADARSAT-2 Dual-Pol ScanSAR data. *IEEE J. Sel. Top. Appl. Earth Obs. Remote Sens.* **2015**, *8*, 1601–1613. [[CrossRef](#)]
52. Haralick, R.M.; Shanmugam, K. Textural features for image classification. *IEEE Syst. Man Cybern. Mag.* **1973**, *6*, 610–621. [[CrossRef](#)]
53. Barber, D.; LeDrew, E. SAR sea ice discrimination using texture statistics—A multivariate approach. *Photogramm. Eng. Remote Sens.* **1991**, *57*, 385–395.
54. Soh, L.K.; Tsatsoulis, C. Texture analysis of SAR sea ice imagery using gray level co-occurrence matrices. *IEEE Trans. Geosci. Remote Sens.* **1999**, *37*, 780–795. [[CrossRef](#)]
55. Lee, J.S.; Wen, J.H.; Ainsworth, T.L.; Chen, K.S.; Chen, A.J. Improved sigma filter for speckle filtering of SAR imagery. *IEEE Trans. Geosci. Remote Sens.* **2009**, *47*, 202–213.
56. Oliver, C.; Quegan, S. *Understanding Synthetic Aperture Radar Images*; SciTech Publishing: Stevenage, UK, 2004.
57. Drinkwater, M.R.; Kwok, R.; Rignot, E.; Israelsson, H.; Onstott, R.G.; Winebrenner, D.P. Potential applications of polarimetry to the classification of sea ice. In *Microwave Remote Sensing of Sea Ice*; Carsey, F.D., Ed.; American Geophysical Union: Washington, DC, USA, 1992; pp. 419–428.
58. Cloude, S.R.; Pottier, E. An entropy based classification scheme for land applications of polarimetric SAR. *IEEE Trans. Geosci. Remote Sens.* **1997**, *35*, 68–78. [[CrossRef](#)]

59. Baraldi, A.; Parmiggiani, F. An investigation of the textural characteristics associated with gray level cooccurrence matrix statistical parameters. *IEEE Trans. Geosci. Remote Sens.* **1995**, *33*, 293–304. [[CrossRef](#)]
60. Hirose, T.K.; McNutt, L.; Paterson, J.S. A Study of Textural and Tonal Information for Classifying Sea Ice from SAR Imagery. In *12th Canadian Symposium on Remote Sensing Geoscience and Remote Sensing Symposium, Proceedings of International Geoscience and Remote Sensing Symposium IGARSS 1989, Vancouver, BC, Canada, 10–14 July 1989*; IEEE: New York, NY, USA, 1989; pp. 747–750.
61. Newsam, S.D.; Kamath, C. *Retrieval Using Texture Features in High Resolution Multi-Spectral Satellite Imagery (No. UCRL-CONF-201981)*; Lawrence Livermore National Laboratory (LLNL): Livermore, CA, USA, 2004.
62. Gong, P.; Marceau, D.J.; Howarth, P.J. A comparison of spatial feature extraction algorithms for land-use classification with SPOT HRV data. *Remote Sens. Environ.* **1992**, *40*, 137–151. [[CrossRef](#)]
63. Cossu, R. Segmentation by means of textural analysis. *Pixel* **1988**, *1*, 21–24.
64. Liew, S.C.; Lim, H.; Kwok, L.K.; Tay, G.K. Texture analysis of SAR images. In *1995 International Geoscience and Remote Sensing Symposium, IGARSS '95. Quantitative Remote Sensing for Science and Applications, Proceedings of International Geoscience and Remote Sensing Symposium IGARSS 1995, Firenze, Italy, 10–14 July 1995*; IEEE: New York, NY, USA, 1995; pp. 1412–1414.
65. Hall-Beyer, M. GLCM Texture: A Tutorial, Version 2.10. 2007. Available online: <https://www.ucalgary.ca/mhallbey/tutorial-glcm-texture> (accessed on 20 January 2018).
66. Breiman, L. Random Forests. *Mach. Learn.* **2001**, *45*, 5–32. [[CrossRef](#)]
67. Millard, K.; Richardson, M. On the importance of training data sample selection in random forest image classification: A case study in peatland ecosystem mapping. *Remote Sens.* **2015**, *7*, 8489–8515. [[CrossRef](#)]
68. Torres, R.; Buck, C.; Guijarro, J.; Suchail, J.L.; Schönerberg, A. The envisat ASAR instrument verification and characterisation. In *Proceedings of the SAR workshop: CEOS Committee on Earth Observation Satellites, Toulouse, France, 26–29 October 1999*; pp. 303–310.
69. Torres, R.; Snoeij, P.; Geudtner, D.; Bibby, D.; Davidson, M.; Attema, E.; Traver, I.N. GMES Sentinel-1 mission. *Remote Sens. Environ.* **2012**, *120*, 9–24. [[CrossRef](#)]
70. Nandan, V.; Scharien, R.; Geldsetzer, T.; Mahmud, M.; Yackel, J.J.; Islam, T.; Duguay, C. Geophysical and atmospheric controls on Ku-, X- and C-band backscatter evolution from a saline snow cover on first-year sea ice from late-winter to pre-early melt. *Remote Sens. Environ.* **2017**, *198*, 425–441. [[CrossRef](#)]
71. Scheuchl, B.; Flett, D.; Caves, R.; Cumming, I. Potential of RADARSAT-2 data for operational sea ice monitoring. *Can. J. Remote Sens.* **2004**, *30*, 448–461. [[CrossRef](#)]
72. Onstott, R.G. SAR and scatterometer signatures of sea ice. In *Microwave Remote Sensing of Sea Ice*; Carsey, F.D., Ed.; American Geophysical Union: Washington, DC, USA, 1992; pp. 73–104.
73. Fung, A.K.; Eom, H.J. Application of a combined rough surface and volume scattering theory to sea ice and snow backscatter. *IEEE Trans. Geosci. Remote Sens.* **1982**, *4*, 528–536. [[CrossRef](#)]
74. Lewis, A.J.; Henderson, F.M.; Holcomb, D.W. Radar fundamentals: the geoscience perspective. In *Principles & Applications of Imaging Radar. Manual of Remote Sensing*, 3rd ed.; Wiley: Hoboken, NJ, USA, 1998; Volume 3, pp. 131–180.
75. Nandan, V.; Geldsetzer, T.; Yackel, J.; Mahmud, M.; Scharien, R.; Howell, S.; King, J.; Ricker, R.; Else, B. Effect of Snow Salinity on CryoSat-2 Arctic First- Year Sea Ice Freeboard Measurements. *Geophys. Res. Lett.* **2017**, *44*. [[CrossRef](#)]
76. Sturm, M.; Liston, G.E.; Benson, C.S.; Holmgren, J. Characteristics and growth of a snowdrift in Arctic Alaska, USA. *Arct. Antarct. Alp. Res.* **2001**, *33*, 319–329. [[CrossRef](#)]
77. Dierking, W.; Dall, J. Sea-ice deformation state from synthetic aperture radar imagery—Part I: Comparison of C- and L-band and different polarization. *IEEE Trans. Geosci. Remote Sens.* **2007**, *45*, 3610–3622. [[CrossRef](#)]

